Inorganic Chemistry
Cite This: Inorg. Chem. 2018, 57, 10791−10801
Article
pubs.acs.org/IC

Crystal Structure of $NaLuW_2O_8·2H_2O$ and Down/Upconversion Luminescence of the Derived $NaLu(WO_4)_2$:Yb/Ln Phosphors (Ln = Ho, Er, Tm)

Xiaofei Shi,[†,‡,§] Maxim S. Molokeev,[∥,⊥,#] Xuejiao Wang,[*,g] Zhihao Wang,[†,‡,§] Qi Zhu,[†,‡] and Ji-Guang Li[*,§]

[†]Key Laboratory for Anisotropy and Texture of Materials, Ministry of Education, Northeastern University, Shenyang, Liaoning 110819, China

[‡]Institute for Ceramics and Powder Metallurgy, School of Materials Science and Engineering, Northeastern University, Shenyang, Liaoning 110819, China

[§]Research Center for Functional Materials, National Institute for Materials Science, Tsukuba, Ibaraki 305-0044, Japan

[∥]Laboratory of Crystal Physics, Kirensky Institute of Physics, Federal Research Center KSC SB RAS, Krasnoyarsk 660036, Russia

[⊥]Department of Physics, Far Eastern State Transport University, Khabarovsk 680021, Russia

[#]Siberian Federal University, Krasnoyarsk 660041, Russia

[g]College of New Energy, Bohai University, Jinzhou, Liaoning 121007, China

Supporting Information

ABSTRACT: Hydrothermally reacting $Lu(NO)_3$ and $Na_2WO_4·2H_2O$ at 200 °C and pH = 8 produced the new compound $NaLuW_2O_8·2H_2O$, which was analyzed via the Rietveld technique to crystallize in the orthorhombic system (space group: *Cmmm*) with cell parameters a = 21.655(1), b = 5.1352(3), and c = 3.6320(2) Å and cell volume V = 403.87(4) Å^3. The crystal structure presents $-(NaO_6)$-$(NaO_6)-$ and $-(LuO_4(H_2O)_2WO_5)$-$(LuO_4(H_2O)_2WO_5)-$ alternating layers linked together by the O^{2-} ion common to NaO_6 octahedron and WO_5 triangle bipyramid. Tetragonal structured and phase-pure $Na(Lu_{0.87}Ln_{0.03}Yb_{0.1})(WO_4)_2$ phosphors (Ln = Ho, Er, and Tm) were directly produced by calcining their $NaLuW_2O_8·2H_2O$ analogous precursors at 600 °C for 2 h, followed by a detailed study of their downconversion/upconversion (DC/UC) photoluminescence. It was shown that the UC luminescence is dominated by a red band at ∼650 nm for Ho^{3+} ($^5F_5 \rightarrow {}^5I_8$ transition), green bands at ∼500−575 nm for Er^{3+} ($^2H_{11/2}/{}^4S_{3/2} \rightarrow {}^4I_{15/2}$ transitions) and a blue band at ∼476 nm for Tm^{3+} ($^1G_4 \rightarrow {}^3H_6$ transition), all via a three-photon process. DC luminescence of the phosphors is characterized by a ∼545 nm green emission for Ho^{3+} ($^5F_4/{}^5S_2 \rightarrow {}^5I_8$ transition, λ_{ex} = 453 nm), ∼500−575 nm green emissions for Er^{3+} ($^2H_{11/2}/{}^4S_{3/2} \rightarrow {}^4I_{15/2}$ transitions, λ_{ex} = 380 nm), and a ∼455 nm blue emission for Tm^{3+} ($^1D_2 \rightarrow {}^3F_4$ transition, λ_{ex} = 360 nm), with CIE chromaticity coordinates of around (0.27, 0.71), (0.26, 0.72), and (0.15, 0.04), respectively.

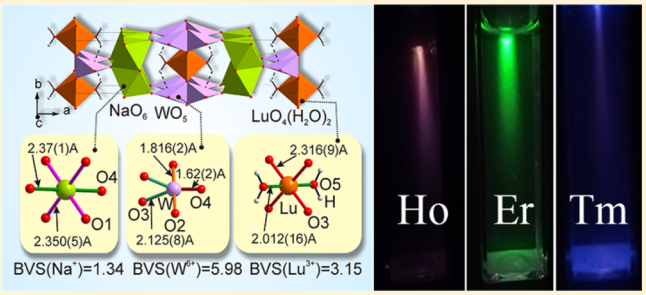

INTRODUCTION

Rare-earth (RE) tungstates have long been a focus of research interest due to their high theoretical densities and excellent resistance to mechanical, chemical, thermal and optical damages. The compounds are currently finding wide applications in the multifaceted fields of solid lasers, quantum electronics, scintillation, and lighting and display.[1−4] Scheelite-type RE tungstates ($ARE(WO_4)_2$, A = an alkali ion) are of special interest because of the outstanding chemical and physical stabilities arising from their compact tetragonal crystal structure (space group: *I*-4).[2,5] The $NaRE(WO_4)_2$ of RE = La, Gd, Lu, and Y, for example, are frequently employed as phosphor hosts, since these RE ions have a vacant (La^{3+} and Y^{3+}), half-filled (Gd^{3+}), or full-filled (Lu^{3+}) 4f shell. The smaller RE ions of Ho, Er, Tm and Yb are especially suitable for $NaLu(WO_4)_2$ doping, since they and Lu have similar ionic radii,[6] which allows for minimal lattice distortion.

A rather limited number of techniques are available for the synthesis of $NaLu(WO_4)_2$ based functional materials, and the most matured one seems to be top-seeded solution growth (TSSG). The technique generally employs $Na_2W_2O_7$ or $Na_2WO_4-Na_2W_2O_7$ as solvent and Na_2CO_3, WO_3 and Ln_2O_3 (Ln = Ho, Er, Tm, Yb, etc.) as raw materials and involves keeping the melt at ∼1100 °C for up to several days.[7−11] Continuous wavelength (CW) and tunable laser

Received: May 24, 2018
Published: August 15, 2018

DOI: 10.1021/acs.inorgchem.8b01427
Inorg. Chem. 2018, 57, 10791−10801

operation has been achieved with the $NaLu_{1-x}Ln_x(WO_4)_2$ crystals fabricated by the TSSG technique (x = 0.05−0.1 for Ln = Tm, 0.005−0.5 for Ln = Yb, and 0.005 for Ln = Ho).[10] Wang et al.[12] produced $NaLu_{1-x}Eu_x(WO_4)_2$ (x = 0.05−1.0) through solid-state reaction of WO_3, $NaHCO_3$, and Lu_2O_3 by preheating and subsequent sintering at 500 and 1000 °C for 4 h, respectively. Gao et al.[13] prepared Tb^{3+}/Pr^{3+} codoped $NaLu(WO_4)_2$ by the sol−gel followed by calcination (800 °C) technique and investigated its temperature sensing property. Wang et al.[14] tempted hydrothermal crystallization of $NaLu_{1-x}Eu_x(WO_4)_2$ (x = 0.4−1.0) microcrystals in the presence of EDTA (neutral solution pH, 180 °C for 12 h) but found that the tetragonal structure cannot be retained when x < 0.4 since the product transformed into a blend of unknown phases, which was ascribed by the authors to be due to the large radius difference between Eu^{3+} and Lu^{3+}. Nonetheless, phase purity of the product seems closely related to the pathway and experimental parameters of synthesis. Zaldo et al.,[15] for example, obtained phase pure Yb:Er:$NaLu(XO_4)_2$ (X = Mo, W) via hydrothermal reaction of $Na_2XO_4 \cdot 2H_2O$ and $Lu(NO_3)_3$ in the absence of any organic additive (pH ∼ 7.5, 170 °C for 24 h). The same authors also achieved multipath synthesis of phase pure Yb:Er:$NaRE(XO_4)_2$ (RE = Y, La, Gd, Lu) through solid-state reaction, hydrothermal reaction and the sol−gel technique, and studied their UC properties by referring to Yb:Er:β-$NaYF_4$.[15]

The sensitizer/activator pairs of Yb^{3+}/RE^{3+} (RE = Ho, Er and Tm) are well-known for their capability of upconversion (UC) luminescence, which has been achieved in various types of host lattices such as fluoride,[1,16,17] oxide,[18−20] phosphate,[1,21] oxysulfate,[22,23] oxysulfide,[24,25] tungstate,[26,27] molybdate,[28] vanadate,[1,29] and so forth. Though the $NaLu(WO_4)_2$ double tungstate of this work has a higher phonon energy ($\hbar\omega$ ∼ 900 cm^{-1})[30,31] than the better known and more widely used RE halides (such as $NaYF_4$, $\hbar\omega$ < 400 cm^{-1})[1,16,17] and oxides (such as Y_2O_3, $\hbar\omega$ ∼ 600 cm^{-1}),[32] a very recent work by Zaldo et al.[15] showed that Yb:Er:$NaRE(XO_4)_2$ phopshors (RE = Y, La, Gd, Lu and X = Mo, W) may have UC efficiencies comparable to Yb:Er:β-$NaYF_4$, which allowed testing equal subcutaneous depths of ex vivo chicken. It was suggsted that the large UC efficiency is mainly benefited from the RE^{3+} multisities and structural disorder that lead to a spatially variable distribution of crystal field potentials around RE^{3+}.[15] Another advantage of Yb/Er-doped $AT(WO_4)_2$ phosphors (A = Li, Na or Ag, T = Y or Ln, and X = W or Mo) is that they have much larger UC ratiometric thermal sensitivities than β-$NaYF_4$:Yb/Er, which is essential for application in UC nanoprobes.[28,33−35] Zheng et al.[35] synthesized laurustinus shaped $NaY(WO_4)_2$:Yb/Er microassemblies of nanosheets via microwave-assisted hydrothermal reaction and demonstrated their potential application as thermal probe. Li et al.[28] synthesized $NaGd(MoO_4)_2$:0.1Yb/xLn UC nanosquares (Ln = Er and Tm, x = 0.005−0.02) via hydrothermal reaction in the presence of oleic acid, and demonstrated an intense green emission of Er^{3+} in the ∼530−553 nm spectral region ($^2H_{11/2}/^4S_{3/2} \rightarrow {}^4I_{15/2}$ transitions) via a two-photon process and a blue emission of Tm^{3+} at ∼477 nm ($^1G_4 \rightarrow {}^3H_6$ transition) via a three-photon mechanism. Yang et al.,[34] on the other hand, hydrothermally crystallized a $NaY(MoO_4)_2$:Yb/Er UC phosphor, discussed its strong green emission (∼536−558 nm; $^2H_{11/2}/^4S_{3/2} \rightarrow {}^4I_{15/2}$ transition) and weak red emission (∼662 nm; $^4F_{9/2} \rightarrow {}^4I_{15/2}$) with a two-photon mechanism, and proposed a novel energy-transfer pathway from Yb^{3+}-MoO_4^{2-} dimers to Er^{3+} for the green enhancement.

Our careful literature survey, however, found that the UC luminescence of Yb^{3+}/Ln^{3+} pairs in $NaLu(WO_4)_2$ was only scarcely studied up to date.[9,10,15] In our effort to synthesize $NaRE(WO_4)_2$ (RE = La−Lu and Y) via hydrothermal reaction of aqueous solutions containing Na_2WO_4 and $RE(NO_3)_3$,[36] the $NaLuW_2O_8 \cdot 2H_2O$ new compound was generated upon reaction at 200 °C and pH = 8, which was shown to be a unique and facile precursor to produce tetragonal structured $NaLu(WO_4)_2$ by calcination at the relatively low temperature of 600 °C. We thus performed systematic crystal structure analysis of the compound and successfully synthesized $NaLu(WO_4)_2$:Yb/Ln phosphors (Ln = Ho, Er, and Tm), followed by detailed analysis of their down/upconversion photoluminescence. It was believed that the structure information provided for $NaLuW_2O_8 \cdot 2H_2O$ may lay the base for future understanding of $NaREW_2O_8 \cdot 2H_2O$ analogues, and the synthesis technique may have the advantages of (1) high chemical purity of the product, since it does not involve any organic surfactant/chelate or nonvolatile alien ions, and (2) uniform distribution of the sensitizer/activator ions in the host lattice, since the $NaLu(WO_4)_2$:Yb/Ln phosphors were directly transformed from their hydrated double tungstate solid-solution precursors, with water vapor as the only exhaust gas, which would benefit luminescence investigation. In addition, the synthetic technique of this work was expected to be extendible to other $NaRE(WO_4)_2$ and even $NaRE(MoO_4)_2$ double molybdates for optical functionalities. In the following sections, we report the materials synthesis, structure determination, and optical properties.

EXPERIMENTAL PROCEDURE

Synthesis Procedure. The tungsten and RE sources are $Na_2WO_4 \cdot 2H_2O$ (analytical grade), $Ho(NO_3)_3 \cdot 6H_2O$ (99.99% pure), and RE_2O_3 (RE = Er−Lu, 99.99% pure). The other reagents of NaOH and nitric acid (HNO_3) are of analytical grade. All the chemicals were purchased from Kanto Chemical Co., Inc. (Tokyo, Japan). The aqueous solution of RE^{3+} (0.1 mol/L) was separately prepared by dissolving the nitrate and oxide in a proper amount of distilled water and nitric acid, respectively, followed by dilution.

In a typical procedure for hydrothermal reaction, 6 mL of $Na_2WO_4 \cdot 2H_2O$ aqueous solution (1.0 mol/L for WO_4^{2-}) was dropwise added into 20 mL of M^{3+} solution (M = $Lu_{0.87}Yb_{0.1}Ln_{0.03}$, 0.1 mol/L for total cations; WO_4^{2-}/M^{3+} = 3:1 molar ratio; Ln = Ho, Er, and Tm, respectively) under magnetic stirring at room temperature, followed by pH adjustment to 8 with dilute NaOH and HNO_3 solutions while keeping the volume of the mixture at 70 mL. After homogenization under constant stirring for 30 min, the mixture was transferred to a Teflon-lined stainless steel autoclave of 100 mL capacity for hydrothermal reaction at 200 °C for 24 h in an electric oven. After natural cooling to room temperature, the hydrothermal product was collected via centrifugation, washed with distilled water three times, rinsed with absolute ethanol once, and then dried in an air oven at 70 °C for 24 h. Calcination of the hydrothermal product was performed in stagnant air at 600 °C for 2 h, with a heating rate of 5 °C/min at the ramp stage.

Characterizations. Phase identification was performed by X-ray diffractometry (XRD, Smart Lab3, Rigaku, Tokyo, Japan) under 40 kV/40 mA, using nickel filtered Cu-Kα radiation (λ = 1.5406 Å) and a scanning speed of 4.0° 2θ min^{-1}. The XRD data for Rietveld refinement were acquired in the step-scan mode with a step size of 0.02° and an accumulation time of 30 s. Profile fitting, crystal structure search and Rietveld refinement were performed with the TOPAS 4.2 software.[37] Morphology and microstructure of the product were analyzed by field emission scanning electron microscopy

DOI: 10.1021/acs.inorgchem.8b01427
Inorg. Chem. 2018, 57, 10791−10801

(FE-SEM, Model S-4800, Hitachi, Tokyo) under an acceleration voltage of 10 kV and transmission electron microscopy (TEM, Model JEM-2100F, JEOL, Tokyo) under 200 kV. Elemental contents of the product were determined via inductively coupled plasma (ICP) spectroscopy for W and Lu on an IRIS Advantage analyzer (Jarrell-Ash Japan, Kyoto), for Na on an SPS3520UV-DD instrument (SII Technologies Inc., Tokyo), and for O via the He gas transportation fusion-thermal conductivity technique on a model TC-436 analyzer (LECO, St. Joseph, MI). Fourier transform infrared spectroscopy (FTIR, Model FT/IR-4200, Jasco, Tokyo) was performed by the standard KBr pellet method. Downconversion and upconversion luminescence of the $NaLu(WO_4)_2$:Yb/RE phosphors was analyzed at room temperature on an FP-6500 fluorospectrophotometer (Jasco) with a 150 W xenon lamp (Jasco) and a 978 nm CW-laser diode (Model KS3−12322−105, BWT Beijing Ltd., Beijing, China) as the excitation sources, respectively.

RESULTS AND DISCUSSION

Characterization and Structure Analysis of $NaLuW_2O_8{\cdot}2H_2O$. XRD analysis yielded sharp reflections, indicating a highly crystalline nature of the hydrothermal product (Figures 1 and S1). Elemental analysis of the same sample

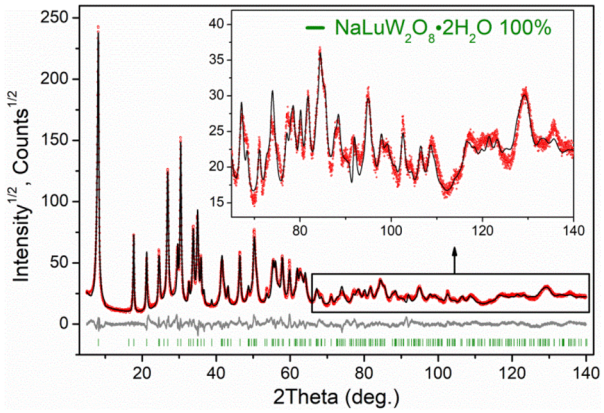

Figure 1. Final Rietveld difference plot of $NaLuW_2O_8{\cdot}2H_2O$. The observed pattern is shown by the black solid line, the calculated data are shown by the red dots, the positions of Bragg reflections are indicated by the green tick marks, and the difference between the results of experiment and calculation is given by the gray line.

found 3.0(±0.1) wt % of Na, 23.8(±0.1) wt % of Lu, 50(±0.1) wt % of W, and 21(±1) wt % of O, well corresponding to a Na: Lu: W: O molar ratio of 1:1.07:2.07:10.07. The results thus suggested a chemical formula of $NaLuW_2O_8{\cdot}2H_2O$ for the product. TG/DSC analysis found weight loss of ∼4.80% for dehydration,[36] which is in good agreement with the water content of 4.93% calculated for $NaLuW_2O_8{\cdot}2H_2O$.

All of the XRD peaks of $NaLuW_2O_8{\cdot}2H_2O$ can be indexed in the *C*-centered orthorhombic cell (Gof = 17.97) using TOPAS 4.2.[30] The systematic absences allows only *Cmmm*, *Cmm*2, and *C*222 space groups, but *Cmmm* was initially used for starting model due to the highest symmetry among them. The structure was solved by modeling in direct space followed by simulated annealing using FOX.[38] One Lu^{3+}, one W^{6+}, and one Na^+ ion were generated and a dynamic population of positions was used for all atoms. The model of the structure was obtained and it was refined using Rietveld refinement in TOPAS 4.2. Difference plot of electron density based on $F_{obs} - F_{calc}$, where F_{obs} and F_{calc} are observed and calculated structural amplitudes, respectively, was used to localize all O^{2-} ions. In total, there are five O^{2-} sites that were localized. Additional refinement with correction intensities on (100) preferred orientation showed decreasing of *R*-factors. Thermal parameter of Na^+ ion was very big after refinement and it was suggested to refine its occupancy factor, which turned out to be ∼0.5. So it was decided to fix it to 0.5. There are four Na^+, two Lu^{3+}, four W^{6+}, and 20 O^{2-} ions in the unit cell, however, taking into account fractional occupancy of Na^+, the formula should be rewritten as $NaLuW_2O_{10}$. Sum of charges gave negative value −4, therefore some of O^{2-} ions should be OH^- or H_2O. Difference electron map of enhanced model after refinement showed two hydrogen atoms near O5 oxygen atom in proper geometry and it was decided that O5 is actually H_2O molecule. Therefore, the chemical formula became $NaLuW_2O_8{\cdot}2H_2O$. Coordinates of H atoms were fixed during refinement and thermal parameters were equal to $1.5 \times B_{iso}(O)$, where $B_{iso}(O)$ is one isotropic thermal parameter for all O ions. Finally, the sum of charge became zero, and the model had reliable geometry and refinement showed low *R*-factors (Figure 1 and Table 1). Coordinates of atoms and main bond lengths are summarized in Tables 2 and S1, respectively. As far as the structure was solved in *Cmmm* space group, it was not necessary to check *Cmm*2 and *C*222 lower space groups. The bond valence sum (BVS) for each ion in this structure was calculated by using the constants from available references[39,40] and taking into account of the fractional occupancy of the ion (Table 2). The BVS values, marked in Figure 2, are close to the

Table 1. Results of Structure Refinements for the $NaLuW_2O_8{\cdot}2H_2O$ Compound[a]

compound	$NaLuW_2O_8{\cdot}2H_2O$
Sp. Gr.	*Cmmm*
a (Å)	21.655 (1)
b (Å)	5.1352 (3)
c (Å)	3.6320 (2)
V (Å^3)	403.87 (4)
Z	2
2θ-interval (deg)	5−140
R_{wp} (%)	10.81
R_p (%)	8.12
R_{exp} (%)	3.19
χ^2	3.38
R_B (%)	3.68

[a] χ^2 was defined as R_{wp}/R_{exp} in the Users' Manual of TOPAS 4.2 software[37].

Table 2. Fractional Atomic Coordinates, Isotropic Displacement Parameters B_{iso} (Å^2) and Atomic Occupancy (occ.) of $NaLuW_2O_8{\cdot}2H_2O$

	x	*y*	*z*	B_{iso}	occ.
Lu	0	0	0.5	0.67 (5)	1
W	0.08306 (7)	0.5	0	1.03 (3)	1
Na	0.25	0.25	0	1.8 (5)	0.5
O1	0.2150 (7)	0	0.5	2.5 (2)	1
O2	0.0841 (8)	0.5	0.5	2.5 (2)	1
O3	0	0.280 (3)	0	2.5 (2)	1
O4	0.1580 (8)	0.5	0	2.5 (2)	1
O5	0.0929 (8)	0	0.5	2.5 (2)	1
H	0.117	0.16	0.5	3.8 (3)	1

DOI: 10.1021/acs.inorgchem.8b01427
Inorg. Chem. 2018, 57, 10791−10801

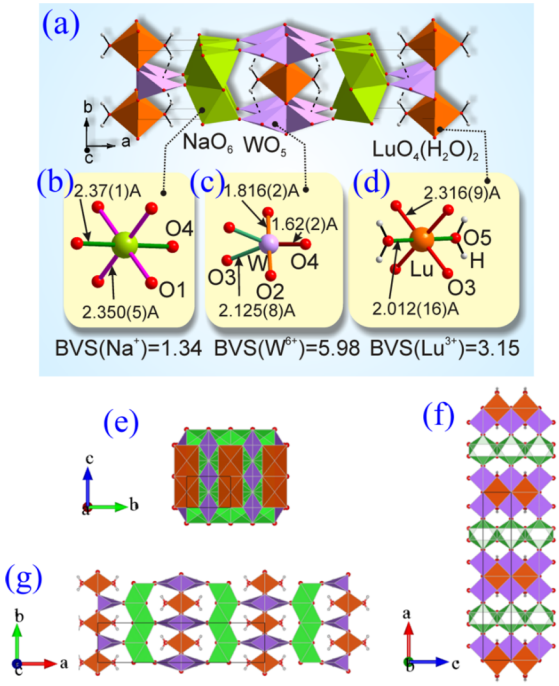

Figure 2. Structure of $NaLuW_2O_8{\cdot}2H_2O$ cell unit (a), cation coordination mode and bond valence sums (BVS) (b–d), and view of the structure along *a*-, *b*-, and *c*-axes (e–g). Hydrogen bonds O–H···O are depicted as dash lines in (a). Purple, green, orange, and red spheres are for W^{6+}, Na^+, Lu^{3+}, and O^{2-}, respectively.

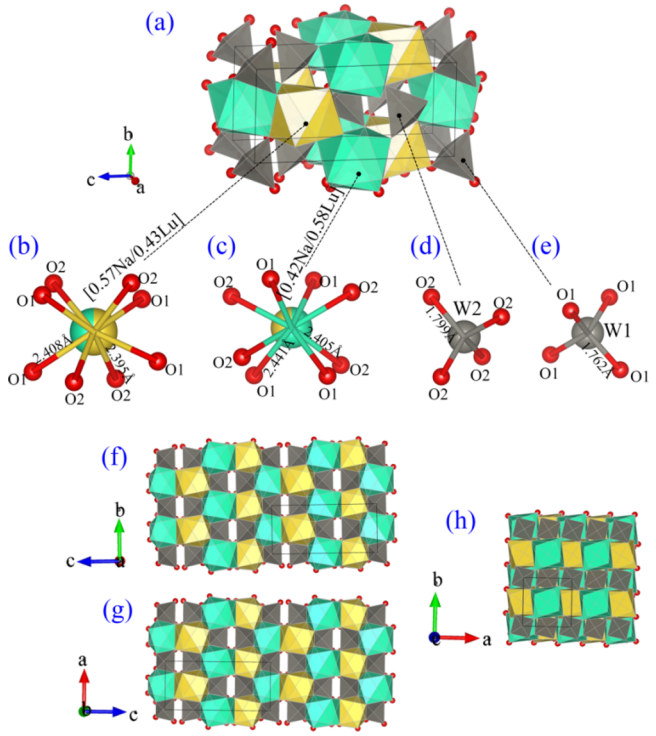

Figure 3. Structure of $NaLu(WO_4)_2$ cell unit (a), cation coordination mode (b–e) and view of the structure along *a*-, *b*-, and *c*-axes (f–h).[7] Gray spheres are for W^{6+} and yellow and green spheres are for [Na/Lu] of different site occupancies.

valences of Na^+, W^{6+}, and Lu^{3+} ions, respectively. While it is a pity that the positions of H atoms could not be directly localized by Rietveld refinement of the XRD pattern, we believe that the outcome of this work may hopefully guide future structure studies and a better understanding of the crystal structure may be achieved with the data taken by neutron diffraction or synchrotron irradiation.

Figure 2 shows the solved crystal structure of $NaLuW_2O_8{\cdot}2H_2O$ (space group *Cmmm*). The Lu^{3+} ion is coordinated by four O^{2-} ions equatorially and two H_2O molecules on the poles of the octahedron. The H_2O molecules are terminal and isolated, but linked with other O atoms through hydrogen bonds forming infinite chain along *b*-axis. The $LuO_4(H_2O)_2$ octahedrons are linked with each other through WO_5 trigonal bipyramids forming 2D layer in *bc* plane. It should be noted that the WO_5 bipyramids are also joined with each other by sharing edges. Each Na^+ ion is 6-fold coordinated with O^{2-}, and the NaO_6 octahedrons are linked with each other by sharing faces and edges to form 2D layer in *bc* plane also. The two layers of···-(NaO_6)-(NaO_6)-··· and···-($LuO_4(H_2O)_2WO_5$)-($LuO_4(H_2O)_2WO_5$)-··· are linked with each other by the O^{2-} ion common to NaO_6 octahedron and WO_5 bipyramid.

The calcination derived tetragonal $NaLu(WO_4)_2$ phase (space group: *I*-4; Figure S2) distinguishes itself from $NaLuW_2O_8{\cdot}2H_2O$ in that (1) Na^+ and Lu^{3+} act as [Na/Lu] pair to form distorted $[Na/Lu]O_8$ square antiprisms, which are distributed over two different lattice sites with the site occupancies of [0.57Na/0.43Lu] (Figure 3b) and [0.42Na/0.58Lu] (Figure 3c), respectively, (2) the $[0.57Na/0.43Lu]O_8$ and $[0.42Na/0.58Lu]O_8$ polyhedrons, alternating with WO_4 tetrahedron in each case, form chains running parallel to *a*- and *b*-axis and are connected via edge-sharing along the *c*-axis (Figure 3f,g,h), and (3) the W^{6+} in the hydration phase is 5-fold coordinated with O^{2-} to form WO_5 trigonal antiprisms, which link together the $LuO_4(H_2O)_2$ and NaO_6 layers along the *a*-axis (Figure 2c,f,g), while that in $NaLu(WO_4)_2$ forms WO_4 tetrahedron and connects the dimeric $[Na/Lu]_2O_{14}$ units along the *c*-axis (Figure 3d–g).

FE-SEM and TEM analysis showed that $NaLuW_2O_8{\cdot}2H_2O$ crystallized as platelets of ~100–300 nm in lateral size (Figure 4a,b). Selective area electron diffraction (SAED) yielded well-arranged diffraction spots, indicating high crystallinity of the sample (Figure 4c). The analyzed *d* spacings of ~2.90, 2.93, and 2.52 Å may correspond to the (1–11), (111), and (020) planes and are in close vicinity to the ~2.94, 2.94, and 2.57 Å derived from the data of Rietveld refinement (Table S2), respectively. The (1–11) and (020) planes would have a dihedral angle of ~125.0°, as calculated from the structure information in Table 1, and is indeed very close to the ~125.3° measured from the SAED pattern (Figure 4c). HR-TEM analysis (Figure 4d) well resolved lattice fringes with the interplanar distances of ~2.91, 2.93, and 2.54 Å, which can be assigned to the (1–11), (111) and (020) planes of orthorhombic $NaLuW_2O_8{\cdot}2H_2O$, respectively. The measured dihedral angles of ~69.6 and 55.0° for (1–11)/(111) and (111)/(020) planes are also in good agreement with those of ~69.8 and 55.1° derived from the results of Rietveld refinement, respectively. The well corresponding TEM and refinement results further confirmed the crystal structure proposed for $NaLuW_2O_8{\cdot}2H_2O$.

Structure and Down/Upconversion Luminescence of $Na(Lu_{0.87}Ln_{0.03}Yb_{0.1})(WO_4)_2$ Phosphors. Figure 5 shows XRD patterns of the Yb/Ln doped hydration phase and 600 °C calcination products, where it can be seen that the former and latter can be fully indexed with $NaLuW_2O_8{\cdot}2H_2O$ (Figure 5a)

DOI: 10.1021/acs.inorgchem.8b01427
Inorg. Chem. 2018, 57, 10791–10801

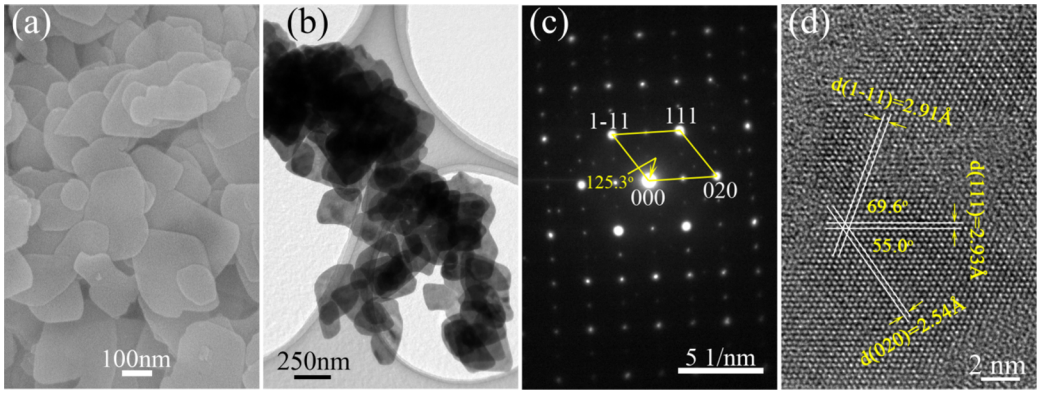

Figure 4. FE-SEM (a) and TEM (b) morphology, SAED pattern (c) and HR-TEM lattice fringes (d) for $NaLuW_2O_8{\cdot}2H_2O$.

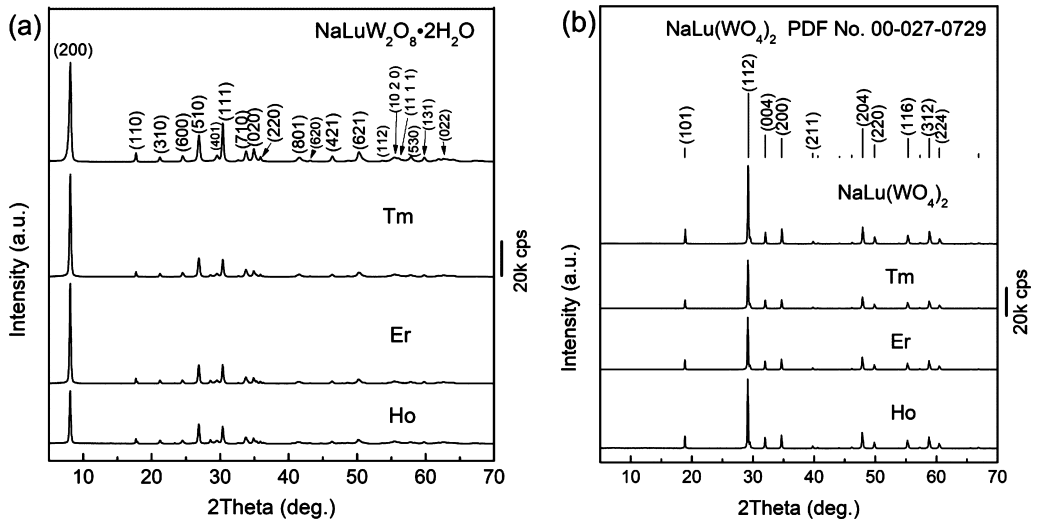

Figure 5. XRD patterns for the as-synthesized $Na(Lu_{0.87}Ln_{0.03}Yb_{0.1})W_2O_8{\cdot}2H_2O$ powders (a) and the products calcined at 600 °C (b). The main diffractions of $NaLuW_2O_8{\cdot}2H_2O$ are indicated in (a) and those of t-$NaLu(WO_4)_2$ in the standard diffraction file are included as bars in (b) for comparison.

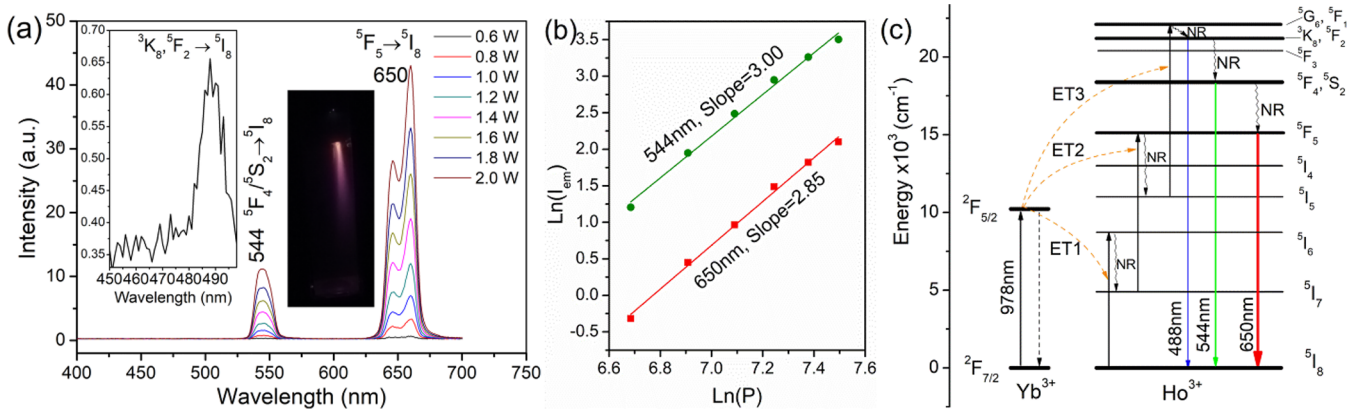

Figure 6. Upconversion luminescence spectra (a), the relationship between $\ln(I_{em})$ and $\ln(P)$ (b), and a scheme showing the energy levels and UC process (c) for the $NaLu(WO_4)_2$:Yb/Ho phosphor. P and I_{em} are the pumping power (in milliwatt) and emission intensity, respectively. The inset photograph in (a) is the appearance of UC luminescence for an aqueous suspension of the phosphor under 2 W laser excitation.

and tetragonal structured $NaLu(WO_4)_2$ (Figure 5b), respectively. It is also seen that the calcination product tends to retain the overall morphology of its precursor, though the thin platelets became less regular in shape, as shown in Figure S3 with the Yb^{3+}/Ho^{3+} doped samples for example. The cell dimension of $NaLu(WO_4)_2$:Yb/Ln is larger than that of $NaLu(WO_4)_2$ in each case and tends to gradually decrease from Ho^{3+} to Tm^{3+} (Table S3 and Figure S4). For 8-fold coordination in tetragonal structured $NaRE(WO_4)_2$, Lu^{3+}, Yb^{3+}, Tm^{3+}, Er^{3+}, and Ho^{3+} ions have the increasing radii of 0.977, 0.985, 0.994, 1.004, and 1.015 Å,[6] respectively, and the Yb^{3+}/Ln^{3+} pair was expected to take the Lu^{3+} site in the crystal

DOI: 10.1021/acs.inorgchem.8b01427
Inorg. Chem. 2018, 57, 10791−10801

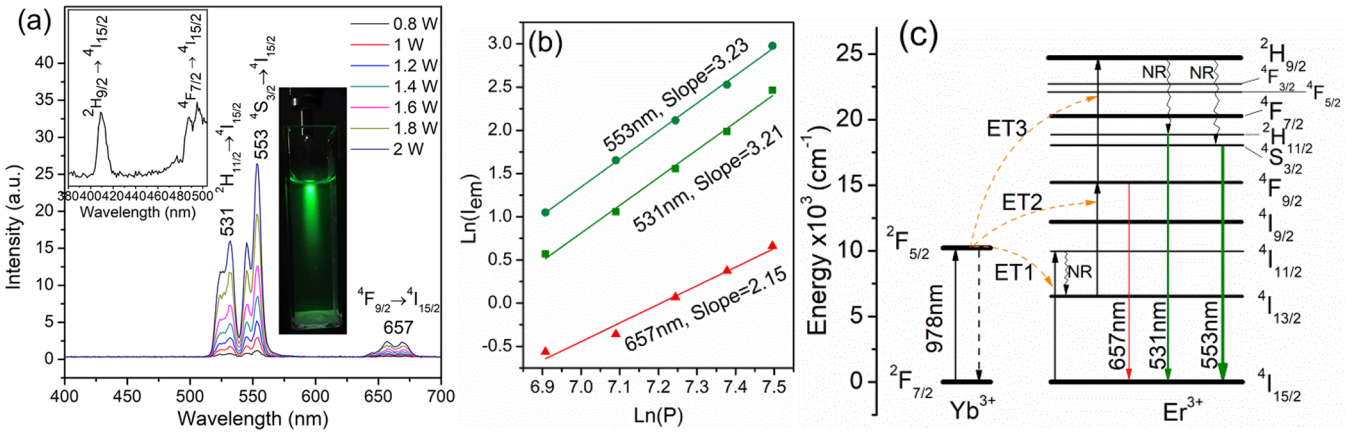

Figure 7. Upconversion luminescence spectra (a), the relationship between $\ln(I_{em})$ and $\ln(P)$ (b), and a scheme showing the energy levels and UC process (c) for the $NaLu(WO_4)_2$:Yb/Er phosphor. P and I_{em} are the pumping power (in milliwatt) and emission intensity in (b), respectively. The inset photograph in (a) is the appearance of UC luminescence for an aqueous suspension of the phosphor under 2 W laser excitation.

lattice. Consequently, doping $NaLu(WO_4)_2$ with Yb^{3+}/Ln^{3+} pair induces lattice expansion, and at the same time, the cell parameter shrinks for a smaller average ionic size of the Yb^{3+}/Ln^{3+} pair. The results are conforming to lanthanide contraction and confirmed the crystallization of solid solution.

Figure 6a shows the UC luminescence spectra of $NaLu(WO_4)_2$:Yb/Ho under 978 nm laser excitation. The emissions at ~544 nm (green) and 650 nm (red) are attributed to the $^5F_4/^5S_2 \rightarrow {}^5I_8$ and $^5F_5 \rightarrow {}^5I_8$ transitions of Ho^{3+},[41,42] respectively, with the latter being predominantly strong. Additionally, negligibly weak blue emission arising from the $^3K_8/^5F_2 \rightarrow {}^5I_8$ transition was resolved at ~488 nm (Figure 6a, the left-hand inset). The UC luminescence is clearly observable with naked eye for an aqueous suspension of the phosphor under 2 W laser pumping (the inset in Figure 6a). The Internationale de l'Eclairage (CIE) chromaticity coordinates determined for the emission slightly drifted from reddish yellow [(0.50, 0.49)] to greenish yellow [(0.47, 0.53)] with increasing excitation power from 0.6 to 2.0 W (Table S4 and Figure S5). The color change agrees with the gradually smaller red to green intensity ratio (I_{650}/I_{544}, Table S5). In general, the number of laser photons required to populate the upper emitting state under unsaturated condition can be obtained from the relation $I_{em} \propto P^n$,[43] where I_{em} is the luminescence intensity, P the pumping power, and n the number of laser photons. Linear fitting of the $\ln(I_{em}) - \ln(P)$ plot (Figure 6b) produced n values of ~3.00 and 2.85 for the ~544 and 650 nm emissions, respectively, which suggested that a three-photon process was involved to generate the observed UC luminescence. The photon reactions may be explained with the energy diagram constructed in Figure 6c as follows: (1) excitation of Yb^{3+} by laser photon [$^2F_{7/2}(Yb^{3+}) + h\nu$(978 nm) $\rightarrow {}^2F_{5/2}(Yb^{3+})$], (2) population of the $^5I_6$ energy level of Ho^{3+} after Yb^{3+} absorbing the first laser photon and transferring energy to Ho^{3+} [ET1; $^2F_{5/2}(Yb^{3+}) + {}^5I_8(Ho^{3+}) \rightarrow {}^2F_{7/2}(Yb^{3+}) + {}^5I_6(Ho^{3+})$], (3) nonradiative relaxation (NR) to the $^5I_7$ level [$^5I_6(Ho^{3+}) \sim {}^5I_7(Ho^{3+})$], followed by excitation to the $^5F_5$ level after Yb^{3+} absorbing the second laser photon and transferring energy to Ho^{3+} [ET2; $^2F_{5/2}(Yb^{3+}) + {}^5I_7(Ho^{3+}) \rightarrow {}^2F_{7/2}(Yb^{3+}) + {}^5F_5(Ho^{3+})$], (4) NR to the $^5I_5$ level [$^5F_5(Ho^{3+}) \sim {}^5I_5(Ho^{3+})$], followed by excitation to the $^5G_6/^5F_1$ state after Yb^{3+} absorbing the third laser photon and transferring energy to Ho^{3+} [ET3; $^2F_{5/2}(Yb^{3+}) + {}^5I_5(Ho^{3+}) \rightarrow {}^2F_{7/2}(Yb^{3+}) + {}^5G_6/{}^5F_1(Ho^{3+})$], and then NR to the $^3K_8/^5F_2$, $^5F_4/^5S_2$, and $^5F_5$ levels, from which the ~488 nm blue, 544 nm green, and 650 nm red emissions were produced upon back jumping of the electrons to the $^5I_8$ ground state, respectively. It seems that the $^5F_5$ level underwent broadening and even splitting under electron population, and thus, the red band split into two sub-bands peaking at ~647 and 660 nm, respectively, with a small energy difference of ~304 cm^{-1}.

Since the $^2F_{5/2} \rightarrow {}^2F_{7/2}$ emission of Yb^{3+} and the $^4I_{15/2} \rightarrow {}^4I_{11/2}$ excitation of Er^{3+} have well-matching energies, the Yb^{3+}/Er^{3+} pair is being frequently studied in various types of host lattices to realize efficient UC luminescence.[21] Under 978 nm laser excitation, the $NaLu(WO_4)_2$:Yb/Er phosphor emits green (~531 and 553 nm, dominantly strong) and red (~657 nm, weak) lights (Figure 7a), which are originated from the $^2H_{11/2}/^4S_{3/2} \rightarrow {}^4I_{15/2}$ and $^4F_{9/2} \rightarrow {}^4I_{15/2}$ transitions of Er^{3+},[43] respectively. Additionally, negligibly weak emissions arising from the $^2H_{9/2} \rightarrow {}^4I_{15/2}$ (~410 nm) and $^4F_{7/2} \rightarrow {}^4I_{15/2}$ (~495 nm) transitions were observed in the magnified spectrum (Figure 7a, the left-hand inset). Under 2 W laser pumping, vivid and strong green luminescence was observed with the naked eyes for an aqueous suspension of the phosphor (the inset in Figure 7a). The emission color determined from the luminescence spectra in the visible-light region (500−700 nm) drifted from the yellowish green [(0.33, 0.62)] to green [(0.25, 0.73)] region in the CIE chromaticity diagram upon raising the excitation power from 0.6 to 2.0 W (Table S4 and Figure S5), which conforms to the gradually larger green to red intensity ratio (I_{531}/I_{657} and I_{553}/I_{657}) under a higher excitation power (Table S5). The green and red emissions were analyzed to have the n values of ~3 and 2, respectively (Figure 7b), and the UC process was proposed in Figure 7c and is detailed below. The Yb^{3+} sensitizer ion in the $^2F_{7/2}$ ground state is populated to the $^2F_{5/2}$ excited state by absorbing a laser photon [$^2F_{7/2}(Yb^{3+}) + h\nu$(978 nm) $\rightarrow {}^2F_{5/2}(Yb^{3+})$]. The Er^{3+} electrons are excited from the $^4I_{15/2}$ ground state to the $^4I_{11/2}$ level by resonant energy transfer from the $^2F_{5/2}$ level of Yb^{3+} to the Er^{3+} activator [ET1; $^4I_{15/2}(Er^{3+}) + {}^2F_{5/2}(Yb^{3+}) \rightarrow {}^4I_{11/2}(Er^{3+}) + {}^2F_{7/2}(Yb^{3+})$]. After NR to the $^4I_{13/2}$ state [$^4I_{11/2}(Er^{3+}) \sim {}^4I_{13/2}(Er^{3+})$], the Er^{3+} electrons are raised to the $^4F_{9/2}$ level by ET of a second laser photon [ET2; $^4I_{13/2}(Er^{3+}) + {}^2F_{5/2}(Yb^{3+}) \rightarrow {}^4F_{9/2}(Er^{3+}) + {}^2F_{7/2}(Yb^{3+})$]. A limited number of the $^4F_{9/2}$ electrons radiatively relax to the $^4I_{15/2}$ ground state, which

DOI: 10.1021/acs.inorgchem.8b01427
Inorg. Chem. 2018, 57, 10791−10801

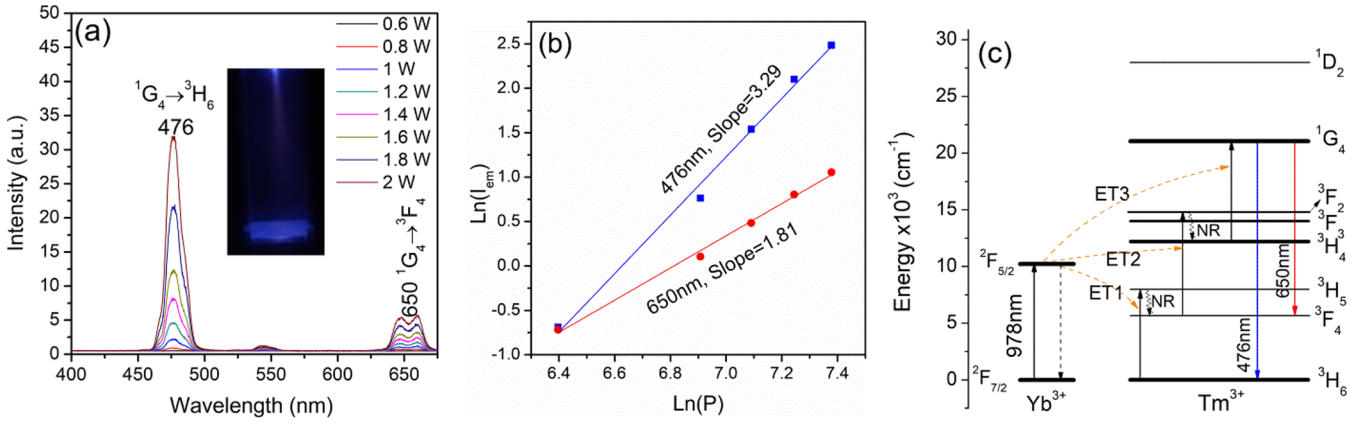

Figure 8. Upconversion luminescence spectra (a), relationship between ln(I_{em}) and ln(P) (b), and a scheme showing the energy levels and UC process (c) for the $NaLu(WO_4)_2$:Yb/Tm phosphor. P and I_{em} are the pumping power (in milliwatt) and emission intensity in (b), respectively. The inset photograph in (a) is the appearance of UC luminescence for an aqueous suspension of the phosphor under 2 W laser excitation.

produces the weak red emission (~657 nm; $^4F_{9/2} \rightarrow {}^4I_{15/2}$). The majority of $^4F_{9/2}$ electrons are further excited to the $^2H_{9/2}$ level with ET of a third laser photon [ET3; $^4F_{9/2}(Er^{3+}) + {}^2F_{5/2}(Yb^{3+}) \rightarrow {}^2H_{9/2}(Er^{3+}) + {}^2F_{7/2}(Yb^{3+})$], from which the observed weak purple emission (~409 nm; $^2H_{9/2} \rightarrow {}^4I_{15/2}$) was generated (Figure 7a, the inset). Significant NR of the $^2H_{9/2}$ electrons to the $^2H_{11/2}$ and $^4S_{3/2}$ states [$^2H_{9/2}(Er^{3+}) \sim {}^2H_{11/2}(Er^{3+})/{}^4S_{3/2}(Er^{3+})$] led to the 531 and 553 nm green emissions upon radiative relaxation to the $^4I_{15/2}$ ground state. The very weak $^4F_{7/2} \rightarrow {}^4I_{15/2}$ emission (~495 nm, the inset in Figure 7a) suggests that the probability of NR from $^2H_{9/2}$ to $^4F_{7/2}$ is rather low.

Under 978 nm laser excitation, the $NaLu(WO_4)_2$:Yb/Tm phosphor exhibits an intense blue emission at ~476 nm and weak red emission at ~650 nm, which correspond to the $^1G_4 \rightarrow {}^3H_6$ and $^1G_4 \rightarrow {}^3F_4$ transitions of Tm^{3+} (Figure 8a), respectively. The negligibly weak green emission at ~545 nm has an energy of ~18.3 × 10^3 cm^{-1}, which could not well match with the energy gap between $^1G_4$ (also $^1D_2$) and any lower energy levels of Tm^{3+}, and thus its occurrence was temporarily ascribed to crystal defects. Under 2-W laser pumping, vivid blue emission of the phosphor suspension was observed with naked eyes (the inset in Figure 8a). The color coordinates of luminescence (400−675 nm) drifted from the white [(0.29, 0.31)] to blue [(0.18, 0.18)] region in the CIE chromaticity diagram with increasing excitation power from 1.0 to 2.0 W (Table S4 and Figure S5). The color change is in agreement with the successively larger blue to red intensity ratio (I_{476}/I_{650}) under a higher excitation power (Table S5). The blue and red emissions are determined to have the n values of ~ 3.29 and 1.81 (Figure 8b), largely conforming to a three- and two-photon process, respectively. As proposed in Figure 8c, the UC process may involve: (1) excitation of Yb^{3+} by laser photon [$^2F_{7/2}(Yb^{3+}) + h\nu$(978 nm) $\rightarrow {}^2F_{5/2}(Yb^{3+})$], (2) population of the $^3H_5$ energy level of Tm^{3+} via energy transfer [ET1; $^2F_{5/2}(Yb^{3+}) + {}^3H_6(Tm^{3+}) \rightarrow {}^2F_{7/2}(Yb^{3+}) + {}^3H_5(Tm^{3+})$], (3) NR to the $^3F_4$ level [$^3H_5(Tm^{3+}) \sim {}^3F_4(Tm^{3+})$], (4) excitation of Tm^{3+} from $^3F_4$ to the $^3F_2$ level with energy transfer of a second laser photon [ET2; $^2F_{5/2}(Yb^{3+}) + {}^3F_4(Tm^{3+}) \rightarrow {}^2F_{7/2}(Yb^{3+}) + {}^3F_2(Tm^{3+})$], (5) NR to the $^3H_4$ level [$^3F_2(Tm^{3+}) \sim {}^3H_4(Tm^{3+})$], followed by excitation to the $^1G_4$ state via energy transfer of a third laser photon [ET3; $^2F_{5/2}(Yb^{3+}) + {}^3H_4(Tm^{3+}) \rightarrow {}^2F_{7/2}(Yb^{3+}) + {}^1G_4(Tm^{3+})$], and (6) radiative relaxation to the $^3H_6$ ground state to produce the blue emission (~476 nm; $^1G_4 \rightarrow {}^3H_6$).[44] The red emission centered at ~650 nm was analyzed to involve a two-photon process (n ~ 1.81) and, thus, its origin was initially assigned to $^3F_2/{}^3F_3 \rightarrow {}^3H_6$ transitions. Further analysis indicated that the energy of this red emission (~15.4 × 10^3 cm^{-1}) presents relatively large deviation from those of the $^3F_2 \rightarrow {}^3H_6$ (~14.8 × 10^3 cm^{-1}) and $^3F_3 \rightarrow {}^3H_6$ (~14.0 × 10^3 cm^{-1}) transitions but well matches with the energy gap (~15.4 × 10^3 cm^{-1}) between the $^1G_4$ and $^3F_4$ levels of Tm^{3+}. The red emission was therefore assigned to $^1G_4 \rightarrow {}^3F_4$ transition. Similar observation and explanation were previously reported by Li et al.[28] and Han et al.[44]

In summary, the $NaLu(WO_4)_2$:Yb/Ln phosphors developed in this work showed UC luminescence dominated by red (~650 nm; $^5F_5 \rightarrow {}^5I_8$ transition), green (~531/553 nm; $^2H_{11/2}/{}^4S_{3/2} \rightarrow {}^4I_{15/2}$ transitions) and blue (~476 nm; $^1G_4 \rightarrow {}^3H_6$ transition) emissions for Ln = Ho, Er and Tm, respectively, all via a three-photon process. The energy process and thus luminescent property of a UC phosphor is known to be significantly affected by the type of host lattice, the contents of sensitizer and activator, distribution uniformity (clustering) of the sensitizer and activator ions, crystallinity, lattice defects, particle/crystallite morphology, excitation power, and the actual lattice site where the dopant ion resides.[1,16,17,45−47] Our literature survey found that Ho^{3+} similarly exhibits strong red emission ($^5F_5 \rightarrow {}^5I_8$) in $NaSrLa(WO_4)_3$[48] and $Y_2(WO_4)_3$,[49] though dominantly stronger green emission ($^5F_4/{}^5S_2 \rightarrow {}^5I_8$) is more frequently encountered in the hosts of β-$NaYF_4$, $BaYF_5$, Y_2O_3, and $NaY(WO_4)_2$.[1,41] Er^{3+} usually shows strong green emission ($^2H_{11/2}/{}^4S_{3/2} \rightarrow {}^4I_{15/2}$) in various types of host lattices, such as β-$NaYF_4$, YF_3, Y_6WO_{12}, $NaGd(WO_4)_2$, $NaY(MoO_4)_2$, and $Y_2(MoO_4)_3$, but predominant red emission ($^4F_{9/2} \rightarrow {}^4I_{15/2}$) was found in α-$NaYF_4$ and $BaYF_5$.[1,27,43,50] Tm^{3+} commonly exhibits strong blue emission ($^1G_4 \rightarrow {}^3H_6$ transition) in the aforementioned hosts. In addition, the UC luminescence mentioned above mostly involves a two-photon mechanism, though a three-photon process was also reported for $Y_2(WO_4)_3$:Yb/Tm.[49] As mentioned earlier, the UC luminescence of a phosphor is substantially affected by a number of factors. While we believe that our $NaLu(WO_4)_2$:Yb/Ln UC phosphors have high chemical/phase purity and uniform distribution of Yb^{3+}/Ln^{3+} pairs in the host lattice, which are benefited from the synthetic technique, and the proposed photon processes are intrinsic to

DOI: 10.1021/acs.inorgchem.8b01427
Inorg. Chem. 2018, 57, 10791−10801

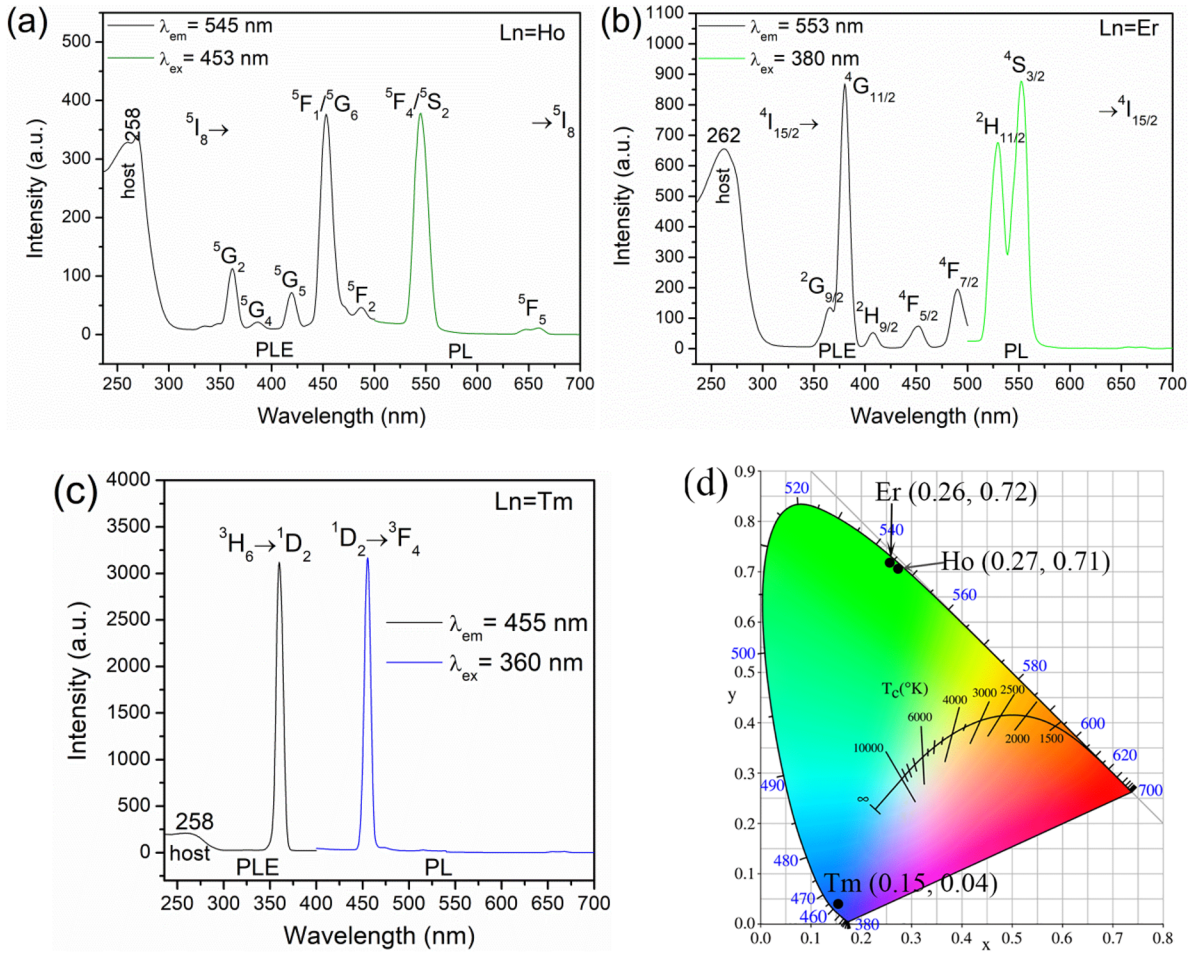

Figure 9. Excitation (left-hand) and downconversion luminescence (right-hand, color lines) spectra of the $NaLu(WO_4)_2$:Yb/Ln phosphors for Ln = Ho (a), Er (b), and Tm (c). (d) CIE chromaticity diagram of the downconversion luminescence.

the phosphors, the decisive factor(s) that led to the different observations between this and previous works yet need to identify. Another point that needs to address is that the laser power used in this work for excitation is relatively high (up to 2 W), and thus heating effect was feared. It is known that heating of a UC phosphor may populate and/or depopulate energy levels of the activator and thus change the photon process and mechanism (number of laser photon n) of UC luminescence.[47] For the Ho^{3+}, Er^{3+}, and Tm^{3+} activators studied in this work, the double-logarithm plot of UC intensity and pump power presented good linear relation in the 0.6−2.0 W power range for each of the investigated emission bands, and therefore, the heating effect may basically be neglected from the photon reactions discussed for the observed UC luminescence.

Figure 9 shows excitation and downconversion luminescence spectra of the $NaLu(WO_4)_2$:Yb/Ln phosphors in the visible light region. The excitation spectrum of Ho^{3+} (Figure 9a), obtained by monitoring the strong 545 nm green emission ($^5F_4/^5S_2 \rightarrow {}^5I_8$), consists of a series of bands ranging from 240 to 500 nm. The broad band located at ∼258 nm can be assigned to host absorption,[51,52] which was observed at ∼264 nm for $NaLu(WO_4)_2$ in this work (Figure S6). The peaks in the 300−500 nm region and located at ∼362, 386, 420, 453, and 487 nm correspond to excitation from the $^5I_8$ ground state to the $^5G_2$, $^5G_4$, $^5G_5$, $^5F_1/^5G_6$, and $^5F_2$ energy levels within the $4f^{10}$ shell of Ho^{3+}, as labeled in the figure,[32,51,53] with the $^5I_8 \rightarrow {}^5F_1/^5G_6$ transition at ∼453 nm being the strongest. The Ho^{3+} phosphor exhibits strong green emission at ∼545 nm ($^5F_4/^5S_2 \rightarrow {}^5I_8$ transition) and weak red emission at ∼650 nm ($^5F_5 \rightarrow {}^5I_8$ transition) under 453 nm excitation. Ho^{3+} shows similar green emission in $CaBi_4Ti_4O_{15}$[54] and Sr_2ScF_7[55] but strong red emission (∼660 nm; $^5F_5 \rightarrow {}^5I_8$) in $Ca_xSr_yBa_{1-x-y}WO_4$[53] and β-$NaYF_4$,[56] which is determined by the composition and site symmetry of the host lattice. The excitation spectrum of Er^{3+} (Figure 9b, λ_{em} = 553 nm) consists of two major components, with the broad band at ∼262 nm arising from host absorption and those at ∼365, 380, 407, 452, and 490 nm attributable to transitions from the $^4I_{15/2}$ ground state to the $^2G_{9/2}$, $^4G_{11/2}$, $^2H_{9/2}$, $^4F_{5/2}$, and $^4F_{7/2}$ energy levels within the $4f^{11}$ shell,[52] respectively. The phosphor exhibits strong green emissions via $^2H_{11/2} \rightarrow {}^4I_{15/2}$ (∼530 nm) and $^4S_{3/2} \rightarrow {}^4I_{15/2}$ (∼553 nm) transitions under 380 nm excitation. Tm^{3+} exhibits host absorption at ∼258 nm and overwhelmingly strong $^3H_6 \rightarrow {}^1D_2$ intra$4f^{12}$ excitation transition at ∼360 nm (λ_{em} = 455 nm), and shows a highly pure blue emission (∼455 nm) via $^1D_2 \rightarrow {}^3F_4$ transition (Figure 9c) under 360 nm excitation.[57] The three phosphors were assayed to have the CIE chromaticity coordinates of around (0.27, 0.71), (0.26, 0.72), and (0.15, 0.04) for Ho^{3+} (green), Er^{3+} (green), and Tm^{3+} (blue), respectively (Figure 9d). The fluorescence lifetime of Ho^{3+}, Er^{3+}, and Tm^{3+} is generally on the μs scale,[53,58,59] which is

DOI: 10.1021/acs.inorgchem.8b01427
Inorg. Chem. 2018, 57, 10791−10801

beyond the measurement limit (ms) of the fluorospectrophotometer of this work.

It was noticed that the ~650 nm red UC emission of Tm^{3+} (Figure 8a) did not appear on the DC luminescence spectrum (Figure 9c). This is due to the different excitation processes for UC and DC luminescence, since the ground state electrons were excited to the $^1G_4$ level with three successive laser photons in the former case while directly to the $^1D_2$ level under 360 nm UV excitation in the latter case. Radiative relaxation of the excited electrons to the same $^3F_4$ level hence produced a red UC emission at ~650 nm but a blue DC emission at ~455 nm. The phenomenon also indicates that the $^1D_2$ electrons hardly relax to the $^1G_4$ level (energy gap between $^1D_2$ and $^1G_4$: $\sim 6.7 \times 10^3$ cm^{-1}). It was also found from the DC excitation spectra (Figure 9a–c) that the main intra4f excitations of Ho^{3+} and Er^{3+} have intensities comparable to host absorption while the $^3H_6 \rightarrow {}^1D_2$ excitation of Tm^{3+} is overwhelmingly stronger than host absorption. This could be understood from the structure of energy levels in the Dieke diagram for RE^{3+}.[60] For Tm^{3+}, the $^1D_2$ level is well isolated from its nearest neighbors and thus the probability of nonradiative relaxation under thermal fluctuation would be negligible, which contributes to the observed much stronger excitation and emission associated with $^1D_2$ (Figure 9c). In contrast, the main excitation levels of Ho^{3+} ($^5F_1/^5G_6$) and Er^{3+} ($^4G_{11/2}$) all have narrowly spaced adjacent energy levels, which readily causes nonradiative relaxation and, thus, substantially lower excitation and emission intensities.

CONCLUSION

The new compound $NaLuW_2O_8{\cdot}2H_2O$ was found to crystallize in the orthorhombic system (space group: *Cmmm*) with cell dimensions of $a = 21.655(1)$, $b = 5.1352(3)$, and $c = 3.6320(2)$ Å and cell volume $V = 403.87(4)$ Å^3. The crystal structure can be viewed as alternating $-(NaO_6)$-$(NaO_6)-$ and $-(LuO_4(H_2O)_2WO_5)$-$(LuO_4(H_2O)_2WO_5)-$ layers linked together by the O^{2-} ion common to NaO_6 octahedron and WO_5 triangle bipyramid. $Na(Lu_{0.87}Ln_{0.03}Yb_{0.1})(WO_4)_2$ phosphors, calcined from their $NaLuW_2O_8{\cdot}2H_2O$ analogous precursors, were found to show upconversion luminescence dominated by a red band at ~650 nm for Ho^{3+}, green bands at ~500–575 nm for Er^{3+} and a blue band at ~476 nm for Tm^{3+}, all via a three-photon process. The three activators also exhibited downconversion luminescence that is characterized by strong bands at ~545 nm for Ho^{3+} (green, $^5F_4/^5S_2 \rightarrow {}^5I_8$ transition; λ_{ex} = 453 nm), 500–575 nm (green, $^2H_{11/2}/^4S_{3/2} \rightarrow {}^4I_{15/2}$ transition; λ_{ex} = 380 nm) for Er^{3+} and 455 nm (blue, $^1D_2 \rightarrow {}^3F_4$ transition; λ_{ex} = 360 nm) for Tm^{3+}.

ASSOCIATED CONTENT

Supporting Information

The Supporting Information is available free of charge on the ACS Publications website at DOI: 10.1021/acs.inorgchem.8b01427.

Structural parameters and XRD data for $NaLuW_2O_8{\cdot}2H_2O$ and the calcination products, CIE chromaticity coordinates and CIE diagram, intensity ratios for the UC luminescence of $Na(Lu_{0.87}Ln_{0.03}Yb_{0.1})(WO_4)_2$, and the PLE/PL spectra of $NaLu(WO_4)_2$. Further details of the crystal structure may be obtained from Fachinformationszentrum Karlsruhe, 76344 Eggenstein-Leopoldshafen, Germany (fax: (+49)7247–808–666; E-mail: crystdata@fiz-karlsruhe.de; http://www.fiz-karlsruhe.de/request_for_deposited_data.html on quoting the deposition number CSD-434413 (PDF).

Accession Codes

CCDC 1845053 contains the supplementary crystallographic data for this paper. These data can be obtained free of charge via www.ccdc.cam.ac.uk/data_request/cif, or by emailing data_request@ccdc.cam.ac.uk, or by contacting The Cambridge Crystallographic Data Centre, 12 Union Road, Cambridge CB2 1EZ, U.K.; fax: +44 1223 336033.

AUTHOR INFORMATION

Corresponding Authors

*Tel.: +81-29-860-4394. E-mail: li.jiguang@nims.go.jp.
*E-mail: wangxuejiao@bhu.edu.cn.

ORCID

Xiaofei Shi: 0000-0001-6934-5427
Qi Zhu: 0000-0001-5513-6309
Ji-Guang Li: 0000-0002-5625-7361

Author Contributions

J.-G.L. conceived the project; X.F.S. carried out the experiments and data analysis; M.S.M. performed crystal structure analysis of $NaLuW_2O_8{\cdot}2H_2O$; J.-G.L. and X.F.S. drafted the manuscript. All the authors were involved in the results discussion and have read and approved the final manuscript.

Notes

The authors declare no competing financial interest.

ACKNOWLEDGMENTS

This work was supported in part by the National Natural Science Foundation of China (Grant Nos. 51672039 and 51702020), the Doctoral Research Fund of Liaoning Province (Grant No. 20170520103), the Fundamental Research Funds for the Central Universities (Grants Nos. N160206001 and N160204008), and Russian Foundation for Basic Research (Grants No. 17-52-53031). X.F.S. acknowledges the financial support from the China Scholarship Council for her overseas Ph.D. study (Contract No. 201606080031).

REFERENCES

(1) Gai, S. L.; Li, C. X.; Yang, P. P.; Lin, J. Recent Progress in Rare Earth Micro/Nanocrystals: Soft Chemical Synthesis, Luminescent Properties, and Biomedical Applications. *Chem. Rev.* **2014**, *114*, 2343–2389.

(2) Kaczmarek, A. M.; Van Deun, R. Rare Earth Tungstate and Molybdate Compounds - from 0D to 3D Architectures. *Chem. Soc. Rev.* **2013**, *42*, 8835–8848.

(3) Durairajan, A.; Thangaraju, D.; Balaji, D.; Moorthy Babu, S. Sol-Gel Synthesis and Characterizations of Crystalline $NaGd(WO_4)_2$ Powder for Anisotropic Transparent Ceramic Laser Application. *Opt. Mater.* **2013**, *35*, 740–743.

(4) Sun, D.-X. Hydrothermal Synthesis of $NaY(WO_4)_2$:Tb^{3+} Powders with Assistance of Surfactant and Luminescence Properties. *J. Mater. Sci.: Mater. Electron* **2015**, *26*, 6892–6896.

(5) Wang, Z. J.; Zhang, Y. L.; Zhong, J. P.; Yao, H. H.; Wang, J.; Wu, M. M.; Meijerink, A. One-Step Synthesis and Luminescence Properties of Tetragonal Double Tungstates Nanocrystals. *Nanoscale* **2016**, *8*, 15486–15489.

(6) Shannon, R. D. Revised Effective Ionic Radii and Systematic Studies of Interatomie Distances in Halides and Chaleogenides. *Acta Crystallogr., Sect. A: Cryst. Phys., Diffr., Theor. Gen. Crystallogr.* **1976**, *32*, 751–767.

DOI: 10.1021/acs.inorgchem.8b01427
Inorg. Chem. 2018, 57, 10791–10801

(7) Han, X. M.; García-Cortés, A.; Serrano, M. D.; Zaldo, C.; Cascales, C. Structural and Thermal Properties of Tetragonal Double Tungstate Crystals Intended for Ytterbium Laser Composites. *Chem. Mater.* **2007**, *19*, 3002−3010.
(8) Han, X.; Fusari, F.; Serrano, M. D.; Lagatsky, A. A.; Cano-Torres, J. M.; Brown, C. T. A.; Zaldo, C.; Sibbett, W. Continuous-Wave Laser Operation of Tm and Ho Co-Doped $NaY(WO_4)_2$ and $NaLu(WO_4)_2$ Crystals. *Opt. Express* **2010**, *18*, 5413−5419.
(9) García-Cortés, A.; Cano-Torres, J. M.; Han, X.; Cascales, C.; Zaldo, C.; Mateos, C. Z.; Rivier, S.; Griebner, U.; Petrov, V.; Valle, V. P. J. Tunable Continuous Wave and Femtosecond Mode-Locked Yb^{3+} Laser Operation in $NaLu(WO_4)_2$. *J. Appl. Phys.* **2007**, *101*, 063110.
(10) Han, X. M.; Cano-Torres, J. M.; Rico, M.; Cascales, C.; Zaldo, C.; Mateos, X.; Rivier, S.; Griebner, U.; Petrov, V. Spectroscopy and Efficient Laser Operation Near 1.95 μm of Tm^{3+} in Disordered $NaLu(WO_4)_2$. *J. Appl. Phys.* **2008**, *103*, 083110.
(11) Zhao, H. Y.; Wang, J. Y.; Zhang, H. J.; Li, J.; Zhang, J. X.; Ling, Z. C.; Xia, H. R. Crystal Growth of Nd:$NaLu(WO_4)_2$. *Mater. Lett.* **2007**, *61*, 4697−4699.
(12) Wang, Z. J.; Zhong, J. P.; Liang, H. B.; Wang, J. Luminescence Properties of Lutetium Based Red-Emitting Phosphor $NaLu(WO_4)_2:Eu^{3+}$. *Opt. Mater. Express* **2013**, *3*, 418−425.
(13) Gao, Y.; Huang, F.; Lin, H.; Zhou, J. C.; Xu, J.; Wang, Y. S. A Novel Optical Thermometry Strategy Based on Diverse Thermal Response from Two Intervalence Charge Transfer States. *Adv. Funct. Mater.* **2016**, *26*, 3139−3145.
(14) Wang, Z. J.; Zhong, J. P.; Jiang, H. X.; Wang, J.; Liang, H. B. Controllable Synthesis of $NaLu(WO_4)_2:Eu^{3+}$ Microcrystal and Luminescence Properties for LEDs. *Cryst. Growth Des.* **2014**, *14*, 3767−3773.
(15) Zaldo, C.; Serrano, M. D.; Han, X.; Cascales, C.; Cantero, M.; Montoliu, L.; Arza, E.; Caiolfa, V. R.; Zamai, M. Efficient Up-Conversion in Yb:Er:$NaT(XO_4)_2$ Thermal Nanoprobes. Imaging of Their Distribution in a Perfused Mouse. *PLoS One* **2017**, *12*, 1−23.
(16) Dong, H.; Sun, L. D.; Yan, C. H. Energy Transfer in Lanthanide Upconversion Studies for Extended Optical Applications. *Chem. Soc. Rev.* **2015**, *44*, 1608−1634.
(17) Wang, X. F.; Liu, Q.; Bu, Y. Y.; Liu, C.-S.; Liu, T.; Yan, X. H. Optical Temperature Sensing of Rare-Earth Ion Doped Phosphors. *RSC Adv.* **2015**, *5*, 86219−86236.
(18) Dong, B.; Liu, D. P.; Wang, X. J.; Yang, T.; Miao, S. M.; Li, C. R. Optical Thermometry through Infrared Excited Green Upconversion Emissions in Er^{3+}-Yb^{3+} Codoped Al_2O_3. *Appl. Phys. Lett.* **2007**, *90*, 181117.
(19) Patra, A.; Friend, C. S.; Kapoor, R.; Prasad, P. N. Fluorescence Upconversion Properties of Er^{3+}-Doped TiO_2 and $BaTiO_3$ Nanocrystallites. *Chem. Mater.* **2003**, *15*, 3650−3655.
(20) Wang, X.; Kong, X. G.; Yu, Y.; Sun, Y. J.; Zhang, H. Effect of Annealing on Upconversion Luminescence of ZnO:Er^{3+} Nanocrystals and High Thermal Sensitivity. *J. Phys. Chem. C* **2007**, *111*, 15119−15124.
(21) Wang, Z. H.; Li, J.-G.; Zhu, Q.; Kim, B.-N.; Sun, X. D. Dicarboxylate Mediated Efficient Morphology/Phase Tailoring of $YPO_4:Ln^{3+}$ Crystals and Investigation of Down-/Up-Conversion Luminescence. *CrystEngComm* **2017**, *19*, 5230−5243.
(22) Chen, G.; Chen, F. S.; Liu, X. H.; Ma, W.; Luo, H. M.; Li, J. H.; Ma, R. Z.; Qiu, G. Z. Hollow Spherical Rare-Earth-Doped Yttrium Oxysulfate: A novel Structure for Upconversion. *Nano Res.* **2014**, *7*, 1093−1102.
(23) Wang, X. J.; Hu, Z. P.; Zhu, Q.; Li, J.-G.; Sun, X. D. $La_2O_2SO_4$:RE/Yb New Phosphors for Near Infrared to Visible and Near Infrared Upconversion Luminescence (RE = Ho, Er, Tm). *J. Am. Ceram. Soc.* **2018**, *101*, 2701.
(24) Li, J.-G.; Wang, X. J.; Liu, W. G.; Zhu, Q.; Li, X. D.; Sun, X. D. $(La_{0.97}RE_{0.01}Yb_{0.02})_2O_2S$ Nanophosphors Converted from Layered Hydroxyl Sulfate and Investigation of Upconversion Photoluminescence (RE = Ho, Er). *Nanoscale Res. Lett.* **2017**, *12*, 508.
(25) Wang, X. J.; Zhu, Q.; Li, J.-G.; Hu, Z. P.; Zhu, G.; Wang, C. La_2O_2S:Tm/Yb as a Novel Phosphor for Highly Pure Near-Infrared Upconversion Luminescence. *Scr. Mater.* **2018**, *149*, 121−124.
(26) Liu, J.; Quinteiro González, E.; Kaczmarek, A. M.; Van Deun, R. Dual-Mode Upconversion and Downshifting White-Light Emitting $Ln^{3+}:Gd_2W_2O_9$ Materials. *New J. Chem.* **2018**, *42*, 2393−2400.
(27) Xue, B.; Sun, J. Y. Synthesis and Tuning Orange to Green Up-Conversion Color in Y_6WO_{12}:Er/Yb Phosphor. *Opt. Mater.* **2013**, *36*, 278−282.
(28) Li, A. M.; Xu, D. K.; Lin, H.; Yang, S. H.; Shao, Y. Z.; Zhang, Y. L. $NaGd(MoO_4)_2$ Nanocrystals with Diverse Morphologies: Controlled Synthesis, Growth Mechanism, Photoluminescence and Thermometric Properties. *Sci. Rep.* **2016**, *6*, 31366.
(29) Sun, Y. J.; Liu, H. J.; Wang, X.; Kong, X. G.; Zhang, H. Optical Spectroscopy and Visible Upconversion Studies of $YVO_4:Er^{3+}$ Nanocrystals Synthesized by a Hydrothermal Process. *Chem. Mater.* **2006**, *18*, 2726−2732.
(30) García-Cortés, A.; Cascales, C.; de Andrés, A.; Zaldo, C.; Zharikov, E. V.; Subbotin, K. A.; Bjurshagen, S.; Pasiskevicius, V.; Rico, M. Raman Scattering and Nd^{3+} Laser Operation in $NaLa(WO_4)_2$. *IEEE J. Quantum Electron.* **2007**, *43*, 157−167.
(31) Voron'ko, Y. K.; Sobol, A. A.; Ushakov, S. N.; Tsymbal, L. I. Raman Spectra and Phase Transformations of $MLn(WO_4)_2$ (M = Na; Ln = La, Gd, Y,Yb) Tungstates. *Inorg. Mater.* **2000**, *36*, 1130−1136.
(32) Yang, J.; Li, C. X.; Quan, Z. W.; Zhang, C. M.; Yang, P. P.; Li, Y. Y.; Yu, C. C.; Lin, J. Self-Assembled 3D Flowerlike Lu_2O_3 and $Lu_2O_3:Ln^{3+}$ (Ln= Eu, Tb, Dy, Pr, Sm, Er, Ho, Tm) Microarchitectures: Ethylene Glycol-Mediated Hydrothermal Synthesis and Luminescent Properties. *J. Phys. Chem. C* **2008**, *112*, 12777−12785.
(33) Li, T.; Guo, C.; Zhou, S.; Duan, C.; Yin, M. Highly Sensitive Optical Thermometry of Yb^{3+}-Er^{3+} Codoped $AgLa(MoO_4)_2$ Green Upconversion Phosphor. *J. Am. Ceram. Soc.* **2015**, *98*, 2812−2816.
(34) Yang, X.; Fu, Z.; Yang, Y.; Zhang, C.; Wu, Z.; Sheng, T.; Srivastava, A. Optical Temperature Sensing Behavior of High-Efficiency Upconversion: Er^{3+}-Yb^{3+} Co-Doped $NaY(MoO_4)_2$ Phosphor. *J. Am. Ceram. Soc.* **2015**, *98*, 2595−2600.
(35) Zheng, H.; Chen, B.; Yu, H.; Zhang, J.; Sun, J.; Li, X.; Sun, M.; Tian, B.; Fu, S.; Zhong, H.; Dong, B.; Hua, R.; Xia, H. Microwave-Assisted Hydrothermal Synthesis and Temperature Sensing Application of Er^{3+}/Yb^{3+} doped $NaY(WO_4)_2$ Microstructures. *J. Colloid Interface Sci.* **2014**, *420*, 27−34.
(36) Shi, X. F.; Li, J.-G.; Wang, X. J.; Zhu, Q.; Kim, B.-N.; Sun, X. D. Facile Hydrothermal Crystallization of $NaLn(WO_4)_2$ (Ln = La-Lu, and Y), Phase/Morphology Evolution, and Photoluminescence. *Sci. Technol. Adv. Mater.* **2017**, *18*, 741−754.
(37) Bruker AXS. *K. TOPAS V4, General Profile and Structure Analysis Software for Powder Diffraction Data, User's Manual*; Bruker, 2008.
(38) Favre-Nicolin, V.; Černý, R. FOX, "Free Objects for Crystallography": A Modular Approach to Ab Initio Structure Determination from Powder Diffraction. *J. Appl. Crystallogr.* **2002**, *35*, 734−743.
(39) Brown, I. D.; Altermatt, D. Bond-Valence Parameters Obtained from a Systematic Analysis of the Inorganic Crystal Structure Database. *Acta Crystallogr., Sect. B: Struct. Sci.* **1985**, *41*, 244−247.
(40) Brese, N. E.; O'Keeffe, M. Bond-Valence Parameters for Solids. *Acta Crystallogr., Sect. B: Struct. Sci.* **1991**, *47*, 192−197.
(41) Huang, S. H.; Wang, D.; Wang, Y.; Wang, L. Z.; Zhang, X.; Yang, P. P. Self-Assembled Three-Dimensional $NaY(WO_4)_2:Ln^{3+}$ Architectures: Hydrothermal Synthesis, Growth Mechanism and Luminescence Properties. *J. Alloys Compd.* **2012**, *529*, 140−147.
(42) Savchuk, O. A.; Carvajal, J. J.; Pujol, M. C.; Barrera, E. W.; Massons, J.; Aguilo, M.; Diaz, F. Ho,Yb:$KLu(WO_4)_2$ Nanoparticles: A Versatile Material for Multiple Thermal Sensing Purposes by Luminescent Thermometry. *J. Phys. Chem. C* **2015**, *119*, 18546−18558.
(43) Liao, J. S.; Nie, L. L.; Wang, Q.; Liu, S. J.; Wen, H.-R.; Wu, J. P. $NaGd(WO_4)_2:Yb^{3+}/Er^{3+}$Phosphors: Hydrothermal Synthesis, Optical

DOI: 10.1021/acs.inorgchem.8b01427
Inorg. Chem. 2018, 57, 10791−10801

Spectroscopy and Green Upconverted Temperature Sensing Behavior. *RSC Adv.* **2016**, *6*, 35152−35159.
(44) Han, Y. H.; Wang, Y.; Huang, S. H.; Jin, F.-L.; Gai, S. L.; Niu, N.; Wang, L. Z.; Yang, P. P. Controlled Synthesis and Luminescence Properties of Doped $NaLa(WO_4)_2$ Microstructures. *J. Ind. Eng. Chem.* **2016**, *34*, 269−277.
(45) Auzel, F. Upconversion and Anti-Stokes Process with f and d Ions in Solids. *Chem. Rev.* **2004**, *104*, 139−173.
(46) Wang, X. F.; Bu, Y. Y.; Yan, X. H.; Cai, P. Q.; Wang, J.; Qin, L.; Vu, T.; Seo, H. J. Detecting the Origin of Luminescence in Er^{3+}-doped hexagonal $Na_{1.5}Gd_{1.5}F_6$ Phosphors. *Opt. Lett.* **2016**, *41*, 5314−5317.
(47) Wang, X. F.; Liu, Q.; Cai, P. Q.; Wang, J.; Qin, L.; Vu, T.; Seo, H. J. Excitation Powder Dependent Optical Temperature Behavior of Er^{3+} Doped Transparent $Sr_{0.69}La_{0.31}F_{2.31}$ Glass Ceramics. *Opt. Express* **2016**, *24*, 17792−17804.
(48) Lim, C. S.; Atuchin, V. V.; Aleksandrovsky, A. S.; Molokeev, M. S. Preparation of $NaSrLa(WO_4)_3$:Ho^{3+}/Yb^{3+} Ternary Tungstates and Their Upconversion Photoluminescence Properties. *Mater. Lett.* **2016**, *181*, 38−41.
(49) Huang, S. H.; Zhang, X.; Wang, L. Z.; Bai, L.; Xu, J.; Li, C. X.; Yang, P. P. Controllable Synthesis and Tunable Luminescence Properties of $Y_2(WO_4)_3$:Ln^{3+} (Ln = Eu, Yb/Er, Yb/Tm and Yb/Ho) 3D Hierarchical Architectures. *Dalton Trans.* **2012**, *41*, 5634−5642.
(50) Lu, W. L.; Cheng, L. H.; Sun, J. S.; Zhong, H. Y.; Li, X. P.; Tian, Y.; Wan, J.; Zheng, Y. F.; Huang, L. B.; Yu, T. T.; Yu, H. Q.; Chen, B. J. The Concentration Effect of Upconversion Luminescence Properties in Er^{3+}/Yb^{3+}-Codoped $Y_2(MoO_4)_3$ Phosphors. *Phys. B* **2010**, *405*, 3284−3288.
(51) Lahoz, F.; Sabalisck, N. P.; Cerdeiras, E.; Mestres, L. Nano-to Millisecond Lifetime Luminescence Properties in $Ln_2(WO_4)_3$ (Ln = La, Ho, Tm and Eu) Microcrystalline Powders with Different Crystal Structures. *J. Alloys Compd.* **2015**, *649*, 1253−1259.
(52) Liu, Y.; Liu, Y. X.; Liu, G. X.; Dong, X. T.; Wang, J. X. Up/Down Conversion, Tunable Photoluminescence and Energy Transfer Properties of $NaLa(WO_4)_2$:Er^{3+},Eu^{3+} Phosphors. *RSC Adv.* **2015**, *5*, 97995−98003.
(53) Li, L. L.; Wu, H.-Y. Host Composition Dependent Tuneable Morphology and Luminescent Property of the $Ca_XSr_YBa_{1-X-Y}WO_4$:RE^{3+} (RE = Pr, Ho, and Er) Phosphors. *J. Alloys Compd.* **2017**, *702*, 106−119.
(54) Xiao, P.; Guo, Y. Q.; Tian, M. J.; Zheng, Q.; Jiang, N.; Wu, X. C.; Xia, Z. G.; Lin, D. M. Improved Ferroelectric/Piezoelectric Properties and Bright Green/UC Red Emission in (Li,Ho)-Doped $CaBi_4Ti_4O_{15}$ Multifunctional Ceramics with Excellent Temperature Stability and Superior Water-Resistance Performance. *Dalton Trans.* **2015**, *44*, 17366−17380.
(55) Zhao, B.; Shen, D. Y.; Yang, J.; Hu, S. S.; Zhou, X. J.; Tang, J. F. Lanthanide-Doped Sr_2ScF_7 Nanocrystals: Controllable Hydrothermal Synthesis, the Growth Mechanism and Tunable Up/Down Conversion Luminescence Properties. *J. Mater. Chem. C* **2017**, *5*, 3264−3275.
(56) Zhuang, J. L.; Yang, X. F.; Fu, J. X.; Liang, C. L.; Wu, M. M.; Wang, J.; Su, Q. Monodispersed β-$NaYF_4$ Mesocrystals: In Situ Ion Exchange and Multicolor Up- and Down-Conversions. *Cryst. Growth Des.* **2013**, *13*, 2292−2297.
(57) Liu, X. L.; Hou, W. H.; Yang, X. Y.; Liang, J. Y. Morphology Controllable Synthesis of $NaLa(WO_4)_2$: the Morphology Dependent Photoluminescent Properties and Single-Phased White Light Emission of $NaLa(WO_4)_2$:Eu^{3+}/Tb^{3+}/Tm^{3+}. *CrystEngComm* **2014**, *16*, 1268.
(58) Feng, H.; Yang, Y.; Cao, H.; Guan, J. Y.; Xu, Y. C. Hydrothermal Synthesis and Luminescence of $NaGd(WO_4)_2$:RE^{3+} (RE = Eu, Tb, Tm) Phosphors. *J. Mater. Sci.: Mater. Electron.* **2015**, *26*, 3129−3133.
(59) Mahalingam, V.; Thirumalai, J.; Krishnan, R.; Mantha, S. Up/Down Conversion Luminescence and Charge Compensation Investigation of $Ca_{0.5}Y_{1-x}(WO_4)_2$:xLn^{3+} (Ln = Pr, Sm, Eu, Tb, Dy, Yb/Er) Phosphors. *Spectrochim. Acta, Part A* **2016**, *152*, 172−180.
(60) Dieke, G. H.; Crosswhite, H. M. The Spectra of the Doubly and Triply Ionized Rare Earths. *Appl. Opt.* **1963**, *2*, 675−686.

DOI: 10.1021/acs.inorgchem.8b01427
Inorg. Chem. 2018, 57, 10791−10801